Multiscale structural control of hydraulic bending in the sensitive plant *Mimosa pudica*

David A. Sleboda[1,2,*], Anja Geitmann[2], Reza Sharif-Naeini[1]

[1]Department of Physiology, McGill University

[2]Department of Plant Science, McGill University

*Corresponding Author

Article Type: Research Article

Subject Areas: Plant Biology, Physics of Living Systems

Abstract

Mechanistic studies of animal and plant motion often focus on the fundamental units of biological actuation: individual motor cells. Recent advances spanning the fields of muscle physiology and biomimetic actuation, however, reveal that important mechanical behaviors also arise at higher levels of organization, driven by the interplay of motor cells with connective tissue networks that guide and control *en masse* deformation. Here we illustrate how a paradigm of cell-driven actuation augmented by a mechanically crucial extracellular matrix is equally applicable to plant pulvini; motor organs evolutionarily distinct from but mechanically analogous to animal muscles. Using pulvini from the sensitive plant *Mimosa pudica,* we visualized anatomical sources of mechanical anisotropy at three hierarchical scales of pulvinus organization, built hydraulic physical models of observed morphologies, and analyzed 3D changes in the shapes of osmotically pressurized pulvini. We find that extracellular guidance controls the direction and extent of turgor-induced pulvinus deformation, an effect that ultimately influences the magnitude, speed, and energetic cost of pulvinus-driven motion. We discuss the relevance of these findings to ongoing work in the fields of muscle physiology and soft robotics, and we situate pulvini within a conceptual framework for understanding the design of biological motor organs generally.

Introduction

Pulvini are sites of joint-like, growth-independent motion in many plants. Visible as fleshy swellings of the bases of petioles, leaves, and individual leaflets, pulvini power active flexion and extension of leafy appendages. Pulvinus-driven movements are thought to provide a variety of adaptive benefits ranging from improving leaf temperature relations to deterring insect and grazing herbivory (Minorsky, 2019), and can occur gradually over the course of hours under the

influence of a circadian rhythm (Mayer et al., 1985) or rapidly as a thigmonastic response to touch, shaking, or wounding of a plant (e.g. Kwan et al. 2013; Song et al. 2014). Anatomically, pulvini consist of a flexible core of vasculature ringed concentrically by a thick cortex of parenchyma cells and a thin enveloping epidermis. The cortex is divided longitudinally into flexor and extensor halves, each containing parenchyma cells that act to bend the organs in flexion or extension, respectively, when turgid. Bulk movement of water from extensor parenchyma to flexor parenchyma has been observed during active bending (Tamiya et al., 1988), indicating that pulvinus deformation is a hydraulic process resulting from mass redistribution of cellular fluid within the organ. Bending is associated with efflux of K^+ and Cl^- ions from extensor cells (Kumon and Suda, 1984), offloading of sugar from vascular elements (Fromm and Eschrich, 1988a), and mass consumption of ATP (Fromm and Eschrich, 1988b), indicating that water movement is ultimately induced by active transport of ions and other osmolites to which water is attracted (Scorza and Dornelas, 2011).

While multiple theoretical models of pulvinus physiology provide insight into the biochemical mechanisms underlying hydraulic bending (e.g. Kagawa and Saito, 2000; Morillon et al., 2001; Kwan et al., 2013; Wang and Li, 2020), important functional properties crucial to a holistic understanding of plant motor biomechanics often emerge at higher levels of organization, influenced by the geometry and material properties of whole plant organs (Forterre et al., 2005, Song et al., 2014). In pulvini, polarized light microscopy suggests that the walls of hydraulic parenchyma cells are reinforced by cellulose microfibrils that selectively restrict radial cell expansion (Mayer et al., 1985). Parenchyma cells have a flattened spheroidal geometry that is conducive to deformation preferentially along the long axis of the pulvinus (Mayer et al., 1985; Koller and Zamski, 2002), and transverse wrinkles in the pulvinus surface have been identified as a morphological feature that increases longitudinal epidermis flexibility without sacrificing circumferential stiffness (Satter et al., 1970; Koller and Zamski, 2002; Song et al., 2014; Mano

and Hasebe, 2021). These structural features have great potential to influence pulvinus physiology by controlling the direction and extent of turgor-induced hydraulic deformation. Despite this, the relative contributions of cell wall ultrastructure, cell geometry, and epidermis morphology to pulvinus mechanics remain unclear, and their collective influence on the energetics of pulvinus-driven motion remains largely unexamined.

To disentangle the contributions of cell wall ultrastructure, cell geometry, and epidermis morphology to the mechanics of hydraulic pulvinus bending, we first visualized each of these structural features in a model organism for the study of rapid plant movement; the sensitive plant *Mimosa pudica*. We then used a series of osmotic perturbations to experimentally swell *M. pudica* pulvini in various states of dissection. This approach allowed us to characterize the influence of each hierarchical feature on hydraulic pulvinus deformation, but also to elucidate mechanical behaviors that emerge from cross-scale interactions between them. Additionally, we hypothesized that one collective impact of multiscale structural constraints could be a reduction in the metabolic cost of pulvinus-driven movement. To test this hypothesis, we built physical models of pulvinus structure from flexible silicone rubber and measured the mechanical pressure-volume work required to induce hydraulic bending. The energetic cost of bending was compared in two models, one with mechanically isotropic walls and one with circumferential hoop reinforcements representing structural anisotropies observed in biological pulvini. A separate physical model of parenchyma cell morphology was built from mylar foil to explore the functional interdependence of parenchymal cell wall reinforcement and cell geometry.

Materials and Methods

Pulvinus morphology, anatomy, and ultrastructure

M. pudica plants were grown from seed in a growth chamber with a 12-hour light-dark cycle at 21-23 C and 60% humidity. Plants were watered approximately once every 3 days and fertilized monthly. The surface morphologies of primary, secondary, and tertiary pulvini, located at the bases of petioles, leaves, and leaflets, respectively, were visualized using a Hitachi TM-1000 scanning electron microscope (SEM). In preparation for SEM, freshly dissected pulvini were dehydrated in a graded series of ethanol, critical point dried, mounted on aluminum stubs with carbon double-sided tape, and sputter coated with a 4 nm layer of gold and palladium.

To visualize cellulose orientation in the cell walls of parenchyma cells, primary pulvini were decellularized using an adapted protocol for the generation of acellular, cellulosic tissue engineering scaffolds from plant material (Adamski et al., 2018). Fresh pulvini were fixed overnight in 4% formaldehyde in 0.1 M phosphate buffer, pH 7.2 (after Kwan et al., 2013) and then bisected longitudinally using a fine razor blade under a stereomicroscope. Fixed, bisected pulvini were immersed in an aqueous solution of 3% NaOH, 5% bleach for approximately 20 hours at room temperature until they appeared uniformly white and translucent under transmitted light illumination, indicating maceration of protein material. Decellularized pulvini were then then gently rinsed in distilled water for 24 hours, dehydrated in 100% ethanol, critical point dried in liquid CO_2, mounted on aluminum stubs with carbon double-sided tape, and sputter coated with a 4 nm layer of gold and palladium. Cut faces of the bisected pulvini were imaged using an environmental scanning electron microscope (FEI Quanta 450 FE-ESEM, FEI Co.) at the McGill University Facility for Electron Microscopy Research, providing lateral views of the internal structure of the decellularized organs.

Cellulose orientation was quantified in high-magnification (~50,000-65,000x) micrographs of parenchymal cell walls using the local gradient function of the Directionality plugin in ImageJ (Liu, 1991). Orientations of identifiable structures in each image were expressed as a histogram with portion of structures observed on the Y axis and angular orientation in degrees on the X axis. All angles were expressed relative to the orientation of the vascular bundle running longitudinally through the core of each pulvinus. The peak of a gaussian curve fit to the collective histogram compiled from all micrographs provided a quantitative metric of the predominant orientation of cellulose microfibrils across samples, and the standard deviation of the gaussian curve provided a metric of histogram width, i.e., the dispersion of microfibril orientations about the predominant angle.

Osmotic perturbations

All osmotic experiments were performed on primary pulvini isolated from the bases of petioles at least two months old. Removal of proximal and distal ends of pulvini yielded approximately cylindrical sections 1000-1500 μm long and 1000-1400 μm wide. Removal of the epidermis from cylindrical pulvinus sections was then accomplished via manual skinning, or rectangular blocks of parenchyma tissue excised from the pulvinus cortex with a fine razor. For consistency, all parenchyma tissue blocks in the current study were excised from the extensor (i.e. ventral or abaxial) cortex of primary pulvini. Thin sections of parenchyma for confocal microscopy were also collected from the extensor cortex by bisecting organs with a pair of razor blades spaced by ~400 μm of double-sided tape.

Dissected pulvinus organs and tissues were soaked in aqueous mannitol solutions of varying concentration to induce osmotic swelling or shrinking. Mannitol is a biologically inert molecule and has been used previously to induce osmotic movement of water into or out of

118 hydraulic plant tissues (Mayer et al., 1985). Cylindrical sections of pulvini, cylindrical sections
119 skinned of their epidermis, and isolated blocks of parenchyma tissue were transferred through
120 graded series of osmotic mannitol baths ranging in concentration from 0 to 878 milliosmoles
121 (mOsm). Following an acclimation time of at least 30 minutes in each bath, samples were
122 imaged in both lateral and ventral views using a digital camera (Zeiss AxioCam MRc, Carl Zeiss
123 AG) mounted on a stereomicroscope (Zeiss SteREO Discovery V8, Carl Zeiss AG). Individual
124 hydraulic parenchyma cells in thin slices of parenchyma were imaged with a laser scanning
125 confocal microscope (LSM710, Carl Zeiss AG) in osmotically neutral (384 mOsm mannitol) and
126 osmotically hypotonic (distilled water) baths. Thin sections were prepared for confocal
127 microscopy by staining briefly (7-9 minutes) with 0.5 mg/ml propidium iodide (PI) in osmotically
128 neutral mannitol. PI binds to cell wall pectin and is a common stain for live imaging of plant
129 anatomical features (Bidhendi et al., 2020). After staining, tissues were rinsed briefly of unbound
130 PI and then excited with a 543 nm Helium-Neon laser at 5% power. Fluorescence emission in a
131 range of 554-711 nm was captured from parenchyma cells deep to the sectioned tissue surface.
132 Cells with a fluorescing nucleus indicating penetration of PI into the cell protoplasm were
133 considered damaged by sectioning and excluded from the study. Optical sections 2.4-6.4 μm
134 thick were captured at the midlines of cells of interest, located by changing focus along the z-
135 axis until the largest apparent cell dimensions were presented in each osmotic bath.

136 Dimensions of dissected pulvini, isolated parenchyma tissues, and individual
137 parenchyma cells were measured using Image J, FIJI (Schindelin et al., 2012). Widths, lengths,
138 and heights of pulvinus preparations measured from stereomicrographs were normalized to
139 tissue dimensions measured in the most hypertonic osmotic bath employed (878 mOsm).
140 Statistically significant changes were identified via two-tailed, one sample t-tests comparing
141 normalized dimensions in the most hypertonic (878 mOsm) and most hypotonic (0 mOsm)
142 bathing solutions. The lengths, heights, widths, lateral perimeters, and frontal perimeters of

individual parenchyma cells measured from confocal micrographs were normalized to dimensions in osmotically neutral baths, and changes between neutral and hypotonic solutions expressed as percentages. Significant changes in cell dimensions were identified as those significantly different from zero in a two tailed one sample t-test.

Physical modeling

To probe the relationship between anatomical constraints and the energetic cost of hydraulic bending, a pair of physical models of gross pulvinus structure were built from flexible silicone rubber (Dragonskin FX Pro, Smooth-On, Inc.). One model was built with approximately isotropic silicone walls while the other was reinforced anisotropically by sewing thread hoop-reinforcements oriented perpendicular to the bending axis of the model. Incremental removal and addition of water from opposing halves of each model simulated redistribution of cellular fluid across flexor and extensor halves of a pulvinus. Hydrostatic pressures developed within models were monitored via pressure gauges (DS-9192 Aneroid Sphygmomanometer Gauge, Prima Care Medical Supplies) connected in series with each model half, and changes in model bending angle were measured from photographs using ImageJ. Mechanical pressure-volume work expended moving fluid and deforming silicone model chambers was calculated as the integral of hydrostatic pressure as a function of volume change. Total pressure-volume work involved in model deformation was calculated as the sum of work done on expanding halves of models during both bending and returning motions, in which models flexed away from and then extended back towards an initial neutral position. This method of total expansion work quantification was chosen because it encompasses all of the mechanical energy loaded into models during one complete cycle of motion, accounting for work done on expanding model halves as well as any contractile work resulting from release of elastic strain energy stored temporarily in stretched silicone walls.

To investigate the contribution of parenchyma cell geometry to anisotropic deformation, a simple model of parenchyma cells was built from heat-sealable mylar foil sheets (Mylar foil bags, Mequer). Eight foil cells with hexagonal polyhedral geometries were assembled and connected in series through their broad faces, approximating the organization of parenchyma cell files in a pulvinus. Foil cells were pneumatically continuous and could be pressurized or depressurized via addition or removal of compressed air. Foil cells were cycled through repeated cycles of expansion and contraction, and the impact of deformation on the structural integrity of the cells observed.

Results

Structural specializations associated with longitudinal flexibility are present across hierarchical spatial scales in *M. pudica* pulvini

Morphological, anatomical, and ultrastructural analyses verified that structural anisotropies were present across hierarchical scales of organization in the sensitive plant *Mimosa pudica*. Across primary, secondary, and tertiary pulvini, epidermal cells enveloping the pulvinus surface were approximately cylindrical in shape with long axes oriented perpendicular to the pulvinus long axis (Fig. 1b,c,d). Perpendicularly oriented epidermal cells were restricted to the immediate regions of pulvini, with neighboring regions of epidermis displaying parallel orientations of cells more typical of elongate plant shoots (Fig. 1e). In accordance with observations of surface wrinkles in live pulvini (Song et al., 2014), surface wrinkles in samples prepared for SEM were oriented predominantly parallel to epidermal cells, i.e., transverse to the pulvinus long axis. Surface wrinkles were confined exclusively to the surfaces of pulvini, and were not apparent on neighboring surfaces of stems, petioles, or leaflets.

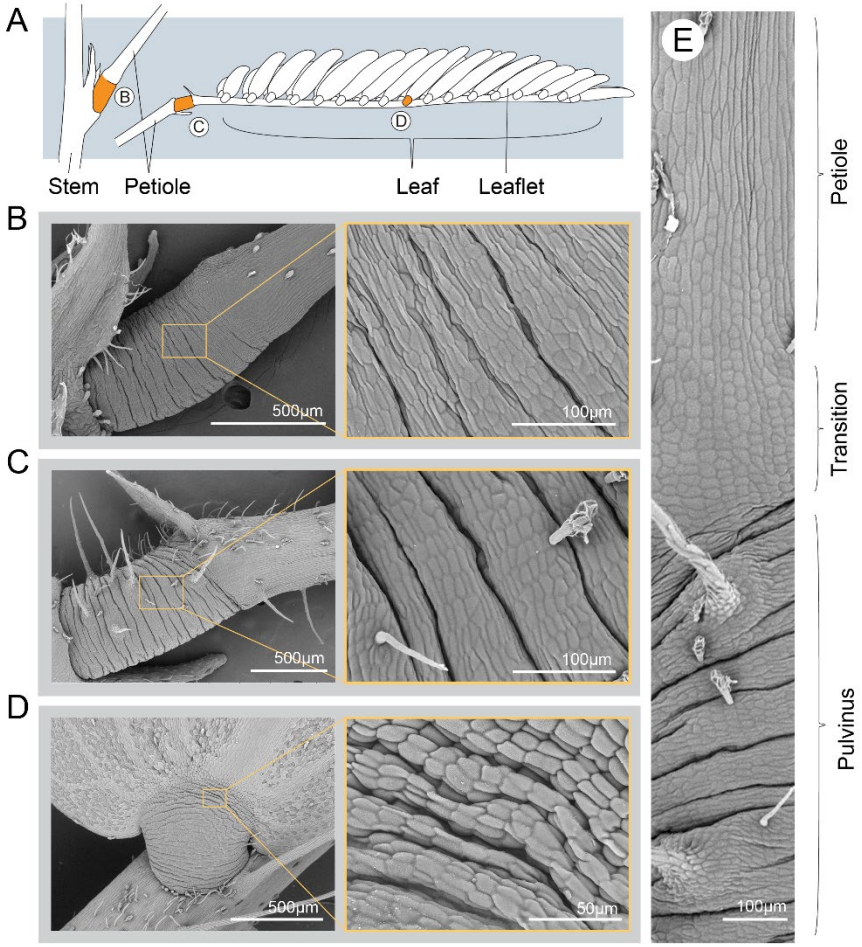

Figure 1: Epidermal cells are oriented perpendicular to the pulvinus long axis and associated with transverse surface wrinkles. [A] Line drawing depicting the locations of primary (B), secondary (C), and tertiary (D) pulvini of *Mimosa pudica*. [B,C,D] Scanning electron micrographs of pulvinus surfaces identified in [A]. Inset micrographs show epidermis architecture at higher magnifications. Epidermis cells bounding pulvini are roughly cylindrical in shape and oriented perpendicular to the long axes of organs. Wrinkles in the epidermis form preferentially parallel to the long axes of epidermis cells. [E] Epidermis cell orientation transitions from perpendicular in the region of the pulvinus to parallel in the region of the petiole (note that the organ long axis is oriented vertically in panel E).

High magnification scanning electron microscopy allowed visualization of individual cellulose microfibrils at the inner surface of parenchymal cell walls. Cellulose microfibrils were aligned primarily dorso-ventrally in the plane of the wall (Fig. 2c,d) with a predominant microfibril orientation of 82.5° ± 29.1° (mean ± SD) relative to the orientation of nearby vasculature (Fig. 2e). Microfibrils were densely arranged, with gaps between adjacent fibrils visible only at the highest magnifications employed.

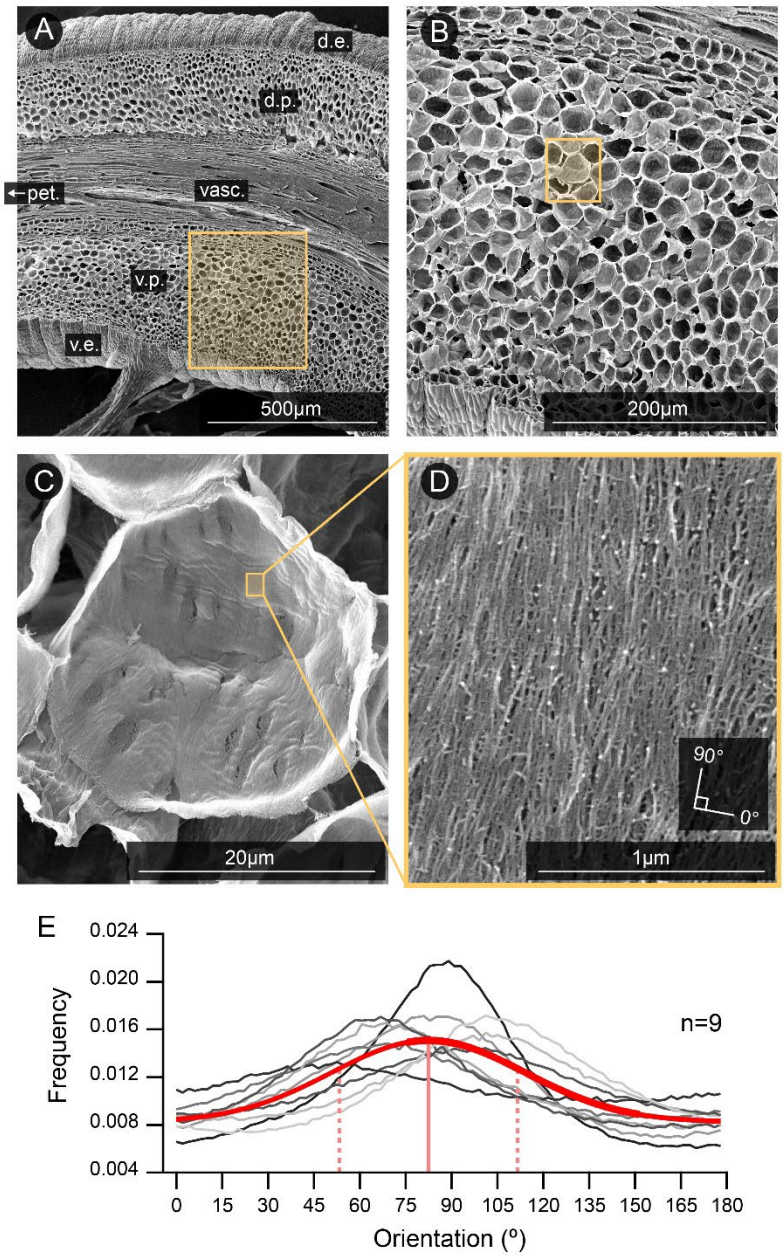

Figure 2: Cellulose microfibrils reinforcing parenchymal cell walls are oriented perpendicular to the pulvinus long axis. [A] Scanning electron micrograph showing a lateral view of a longitudinally bisected primary pulvinus. Protoplasts have been removed chemically to reveal cell wall architecture. Labels indicate dorsal (adaxial) epidermis (d.e.), dorsal parenchyma (d.p.), vasculature (vasc.), ventral (abaxial) parenchyma (v.p.), and ventral epidermis (v.e.). Organ is oriented with petiole (pet.; not visible) left of the frame. [B] Magnified view of the highlighted region in A showing ventral parenchyma bounded by vasculature and ventral epidermis. [C] Magnified view of the highlighted region in B showing the inner face of one parenchymal cell wall. [D] High magnification view of the highlighted region in C showing cellulose microfibrils running primarily dorso-ventrally in the plane of the cell wall. Fiber angles are described relative to the long axis of nearby vasculature (defined as 0°) with 90° indicating a perpendicular orientation. [E] Histograms showing distributions of fiber orientations in 9 cells from 4 pulvini. Each gray trace shows the distribution of fiber angles in a high magnification scanning electron micrograph similar to D. A gaussian curve (solid red trace) fit to all histograms indicates a predominant fiber orientation of 82.5 degrees (solid vertical line) with a standard deviation of ± 29.1 degrees (dotted vertical lines). Source data file provides tabulated histogram values.

221 **Osmotic swelling occurs anisotropically across scales of pulvinus organization**

222 Osmotic swelling experiments revealed the influence of structural specializations on the
223 mechanical behavior of *M. pudica* pulvini. Imposed osmotic swelling resulted in anisotropic
224 deformation of pulvinus tissues and cells at all hierarchical levels studied. Across a graded
225 series of osmotic baths ranging from 0 to 878 mOsm, cylindrical sections of pulvinus organ with
226 an encompassing epidermis (Fig. 3c) displayed a 15.26 ± 2.75% (mean ± standard deviation
227 (SD), $p < 0.01$) change in length without significant changes in either width (1.74 ± 1.83%, $p =$
228 0.11) or height (1.02 ± 2.42%, $p= 0.10$). Cylindrical pulvinus sections skinned of their epidermis
229 (Fig. 3d) varied in length 17.70 ± 4.26% ($p < 0.01$), increased marginally in width (2.91 ± 1.98%,
230 $p < 0.01$), and displayed increased variation in height (7.80 ± 8.55%, $p = 0.05$). Isolated blocks
231 of parenchyma tissue dissected free of epidermis and vasculature (Fig. 3e) changed in length
232 26.16 ± 3.15% ($p < 0.01$) without statistically significant changes in either width (-1.39 ± 2.40%,
233 $p = 0.26$) or height (3.76 ± 5.75%, $p = 0.22$). The increased variation in the height of cylindrical
234 organ sections skinned of their epidermis was attributable to a tendency for elongating
235 parenchyma tissues to bow dorsally and ventrally away from the stiff central vasculature of the
236 pulvinus organ. This bowing resulted in skinned pulvinus sections adopting spindle-shaped
237 lateral profiles reminiscent of rugby or American footballs when swollen osmotically (Fig. 3f and
238 Fig. 3- Video 2). Isolated blocks of parenchyma tissue dissected free of their anatomical context
239 displayed the largest changes in length of all pulvinus preparations studied, supporting the
240 notion that the stiff central vasculature resists longitudinal expansion of the pulvinus.
241

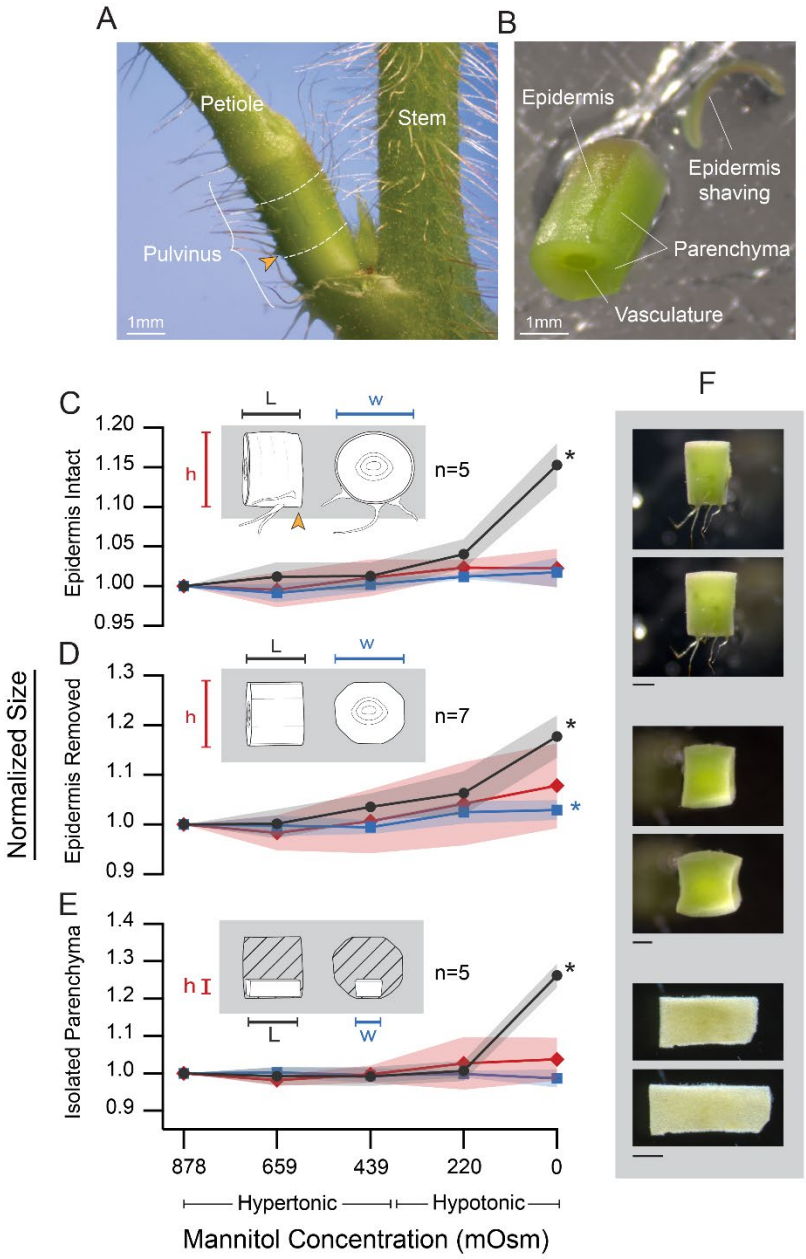

Figure 3: Nonuniform osmotic swelling of pulvini reveals multiscale control of hydraulic deformation. [A] Lateral view of an intact *Mimosa pudica* primary pulvinus with flanking leaves removed. Dashed white lines illustrate cross-sectional cuts used to isolate a cylindrical section of pulvinus. Orange arrowheads in A and C indicate proximal, ventral corner of section. [B] Isolated cylindrical section of pulvinus with epidermis partially removed to illustrate skinning technique. [C, D, E] Effect of graded osmotic bathing solutions on the length (L, black circles), cross-sectional width (w, blue squares), and height (h, red diamonds) of excised pulvinus sections. Inset line drawings depict dimensions and typical morphologies in lateral and cross-sectional views. Graph markers are means ± SD normalized to tissue dimensions in the most hypertonic bathing solution (878 mOsm). Asterisks denote values significantly different from 1.0 in the most hypotonic bathing solution (0 mOsm). [C] Isolated pulvinus sections expand longitudinally in increasingly hypotonic bathing solutions with negligible change in width or height. [D] Sections manually skinned of their epidermis expand primarily in length but display a small increase in width and increased variability in height. [E] Isolated blocks of parenchyma tissue expand longitudinally with negligible change in width or height. Sample sizes (n) for each condition are noted beside inset illustrations. [F] Representative images illustrating shape changes of pulvinus sections in each state of dissection. Upper and lower images of each pair display sample shape in hypertonic and hypotonic baths, respectively. Scale bars 500 µm. Associated videos show timelapses of osmotic deformations. Source data file provides tabulated dimensions in each osmotic condition.

The bias towards longitudinal deformation displayed by pulvinus organ sections and tissues persisted at the level of individual pulvinus parenchyma cells. The geometries of individual parenchyma cells were observable in both scanning electron micrographs of macerated pulvini (Fig. 2) and confocal micrographs of live parenchyma tissue (Fig. 4). Parenchyma cells were polyhedral spheroids approximately hexagonal in cross section. The lateral shape of live parenchyma cells was strongly dependent on the concentration of the osmotic solution in which they were maintained. In isotonic solution, cells were typically flattened slightly along their longitudinal axes; similar in shape to lentils with broad faces oriented perpendicular to the pulvinus long axis. Individual parenchyma cells (Fig. 4a) visualized within blocks of parenchyma transferred from osmotically neutral (384 mOsm) to osmotically hypotonic (0 mOsm) bathing solutions displayed a marginal change in height of 1.78 ± 2.99% (mean ± SD, $p < 0.01$), did not change significantly in width (-0.56 ± 1.88%, $p = 0.13$), but displayed a relatively large increase in length of 14.48 ± 5.07% ($p < 0.01$; Fig. 4b). Measurements of frontal and lateral cell perimeters revealed anisotropy in the amount of cell wall distension that occurred during osmotic expansion. Lateral cell perimeter, measured parallel to the organ long axis, increased 6.87 ± 3.10% ($p < 0.01$) while frontal cell perimeter, measured in cross section perpendicular to the organ long axis, changed only marginally (0.96 ± 1.41%, $p < 0.01$). Following transfer to hypotonic bathing solutions, lateral cell profiles extended without changes in cross-sectional shape, indicating deformation of longitudinally flattened cells towards more perfectly spherical polyhedral geometries under increased turgor.

313

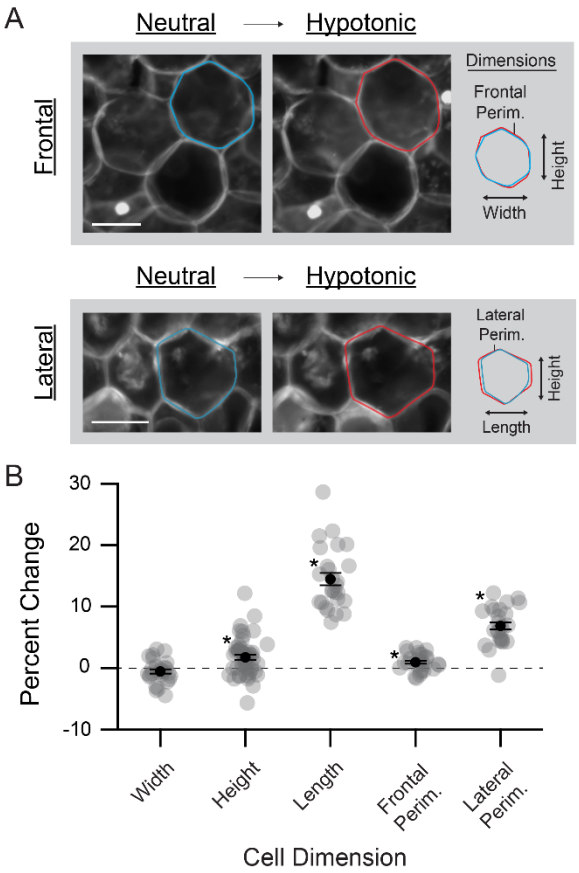

314 Figure 4: Nonuniform osmotic swelling of pulvinus parenchyma cells reveals mechanical anisotropy in the
315 cell wall. [A] Confocal micrographs of parenchyma tissue imaged in osmotically isotonic (384 mOsm) and
316 hypotonic (distilled H_2O) bathing solutions. Representative micrographs show cell morphology as seen in
317 frontal and lateral views. All scale bars 20 µm. Inset line drawings illustrate changes in cell shape
318 between osmotic solutions. [B] Effect of osmotic swelling on frontal and lateral dimensions of 53 cells
319 measured over 8 experimental trials. Gray dots represent percent changes in cell dimensions following
320 transfer from neutral to hypotonic bath. Black markers represent means ± standard errors. Asterisks
321 denote percent changes significantly different from zero ($p<0.05$). Source data file provides tabulated
322 dimensions in each osmotic condition.

323

Physical models illustrate mechanisms of anisotropic deformation and their influence on energetic efficiency

Silicone models of abstracted pulvinus structure showed the potential for passive structural constraints to influence the mechanics and energetics of hydraulic bending. Silicone models of pulvini qualitatively mimicked the hydraulic motor abilities of *Mimosa pudica,* displaying long axis bending in response to redistribution of internal fluid (Fig. 5a,b). Hoop reinforcements oriented perpendicular to the model long axis inhibited radial expansion of silicone walls and reduced the volume of fluid required to effect bending motion (Fig. 5d). Fluid pressures developed within the reinforced silicone model were higher than those in the unreinforced models (Fig. 5e); however, the energetic cost of effecting angle change via transfer of pressurized fluid across model chambers was ultimately lower in the reinforced model (Fig. 5f). Total energy input to complete one cycle of motion was 51.3 mJ for 23 degrees of bending of the unreinforced model (~2.2 mJ per degree of bending), compared to 29.7 mJ for 29 degrees of bending of the reinforced model (~1.0 mJ per degree of bending).

Foil models of abstracted parenchyma cells illustrated the influence of cell geometry on anisotropic swelling behavior. Foil models were composed of mechanically isotropic and inextensible walls. Though their walls lacked directional reinforcements, the models qualitatively mimicked the anisotropic expansion of parenchyma tissue through purely geometrical means. When pressurized internally, polyhedral, disk-shaped cells expanded longitudinally with negligible radial expansion (Fig. 6b). It was noted, however, that the inextensible foil cells were prone to kinking at their perimeters when pressurized internally, typically resulting in rupture of the model cells following repeated cycles of expansion and contraction (Fig. 6c).

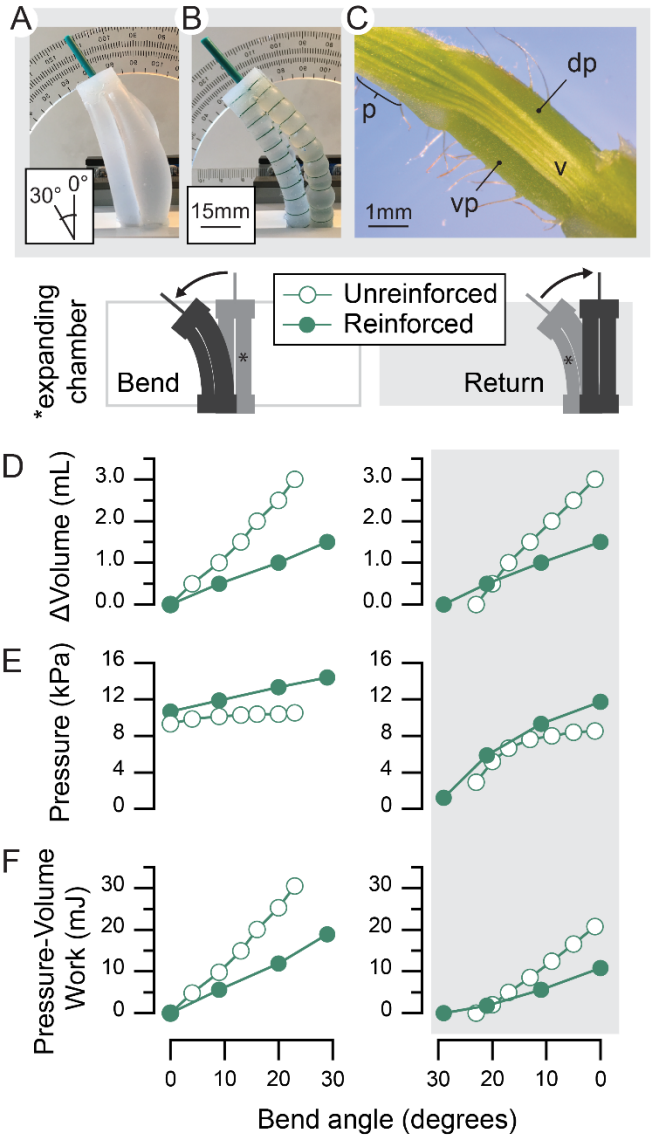

Figure 5: Physical models of gross pulvinus structure illustrate the influence of shape constraints on hydraulic and energetic bending efficiencies. [A] An abstracted physical model of a pulvinus made of flexible silicone rubber. Transfer of water from one half of the model to the other causes long-axis bending. [B] Sewing thread hoop reinforcements prevent radial expansion of pressurized model chambers. [C] Lateral view of a longitudinally bisected primary pulvinus organ. Opposing silicone chambers of each model represent dorsal (dp) and ventral (vp) parenchyma cell groups, respectively. Pulvinus vasculature (v) and petiole (p) indicated for clarity. [D, E, F] Comparison of fluid volume, pressure, and work required to effect a change in bending angle in an unreinforced (open circles) and a hoop-reinforced (filled circles) physical model. Graphs in left-hand column describe bending phase of motion for each model, while graphs in shaded right-hand column describe return phase of motion. Asterisks in inset line drawings indicate expanding halves of models in each movement phase. [D] The volume of fluid required to effect angle change is reduced in the reinforced model relative to the unreinforced model during both bend and return motions. [E] Fluid pressures measured from expanding model compartments are elevated in the reinforced model. [F] Mechanical work (the integral of pressure and volume changes) expended transferring water across model compartments is ultimately lower for the reinforced model during both bending and returning phases of motion. Associated videos show models bending hydraulically.

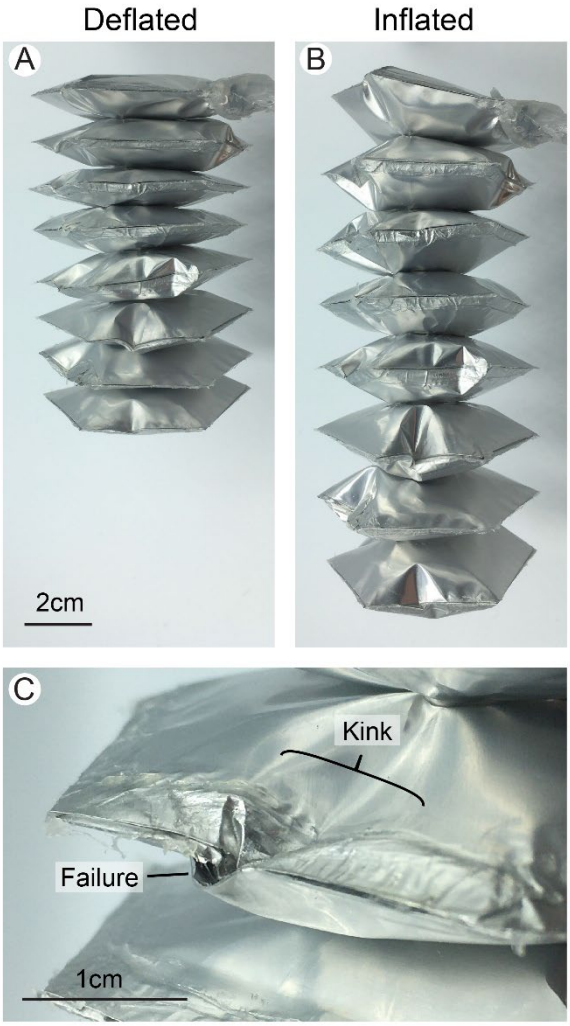

Figure 6: A mylar foil model of parenchyma cells demonstrates the influence of cell geometry on mechanical anisotropy. [A] The model is composed of eight flattened, hexagonal cells connected serially. Foil cell walls lack directional reinforcements and are inextensible and materially isotropic. [B] When pressurized internally, cells extend longitudinally with negligible change in radius. [C] Kinks formed in inextensible cell walls result in material failure and loss of pressurization following repeated cycles of expansion and contraction. Associated video shows pneumatic expansion of the model.

372 **Discussion**

373 The hydraulic nature of pulvinus-driven movement has been recognized since the 1800s
374 and is discussed in Darwin's *The Power of Movement in Plants* (Darwin and Darwin, 1880).
375 However, a holistic understanding of the mechanisms by which pulvini transform non-directional
376 cellular turgor pressures into anisotropic, directed movement of their parts has remained
377 elusive. Here we demonstrate that in the pulvini of the sensitive plant *Mimosa pudica,* a suite of
378 hierarchically arranged ultrastructural, anatomical, and morphological specializations produce
379 mechanical anisotropy at subcellular, cellular, and tissue levels of pulvinus organization. These
380 specializations are perpendicular orientations of cellulose microfibrils in parenchymal cell walls,
381 longitudinally-flattened spheroidal geometries of parenchyma cells, and perpendicular
382 orientations of epidermis cells in the region of the pulvinus. The salient finding of the current
383 work is that concerted deformation of pulvini emerges from the cross-scale interaction of these
384 hierarchically arranged components, rather than from the independent contributions of any
385 individual component acting in isolation. Together, they compose a multiscale structural system
386 that guides turgor-induced deformation across scales of pulvinus organization. The silicone
387 physical models employed in the current study suggest that one overall impact of this multiscale
388 guidance system is a decrease in the volume of fluid transfer required to induce hydraulic
389 actuation; a feature that ultimately reduces the energetic cost of pulvinus-driven movement.

390

391 **Functional interdependence of cell wall ultrastructure and cell geometry**

392 Through ultrastructural analysis of parenchyma cell walls, we observed cellulose
393 microfibrils in parenchymal cell walls oriented predominantly transverse to the long axes of
394 pulvini. Cellulose microfibrils are crystalline structures composed of closely packed chains of
395 parallelly-oriented cellulose molecules (Brett, 2000) and display high tensile strengths and

396 longitudinal stiffnesses of approximately 1 GPa and 130 GPa respectively (Gibson, 2012).
397 Cellulose microfibrils function as the primary mechanical component of the plant cell wall,
398 ultimately providing the tensile strength needed to balance large intracellular turgor pressures
399 ranging from 0.4-0.8 MPa in typical hydrated plant tissues (Taiz et al., 2015) to over 1 MPa in
400 some specialized plant cells (Franks, 2003). Anisotropic patterns of cellulose reinforcement are
401 not unique to pulvini; cellulose orientation is actively controlled by the action of cellulose
402 synthase complexes that extrude cellulose microfibrils into the extracellular space (Brett, 2000),
403 and anisotropic cellulose deposition is the primary means by which mechanical anisotropy is
404 produced and maintained in plant cell walls. The interplay of intracellular pressure and cell wall
405 anisotropy ultimately governs the direction of irreversible turgor induced shape changes in
406 growing cells (Baskin, 2005) and underlies the development of complex non-spherical
407 morphologies (Bidhendi and Geitmann, 2016). Interactions between cell wall anisotropy and
408 turgor pressure have also been shown to underlie reversible deformation of certain mature plant
409 cell types. The hydraulic guard cells flanking stomatal pores, for example, are reinforced by
410 cellulose microfibrils oriented primarily perpendicular to the guard cell long axis (Galatis and
411 Apostolakos, 2004). The perpendicular orientation of microfibrils inhibits radial expansion of
412 guard cells while permitting elongation during hydraulic expansion, ultimately facilitating the
413 microscopic outward bowing of guard cells that opens the stomatal pore (Aylor et al., 1973).
414 Analogous to the effect of cellulose anisotropy in stomatal guard cells, our results verify that
415 cellulose microfibrils selectively restrict radial expansion of parenchymal cell walls in the pulvini
416 of *M. pudica*, resulting in anisotropic longitudinal cell wall deformation in response to turgor
417 change.

418 While deformation of parenchyma cell walls occurs preferentially along the long axis of
419 pulvini, our results indicate that direct stretching of the cell wall cannot account for all of the
420 longitudinal cell deformation observed in the current study. Following transfer from isotonic to

421 hypotonic bathing solution, the average length of parenchyma cells increased by 14.50 ± 5.07%
422 (mean ± SD); however, the lateral perimeters of these same parenchyma cells increased by
423 only 6.87 ± 3.10%, indicating that direct stretching of the cell wall accounts for less than half of
424 longitudinal cell deformation on average, even under the assumption that all cell wall distension
425 contributes exclusively to elongation. Geometric deformation of cells from longitudinally
426 flattened lateral profiles towards more perfectly spherical lateral profiles accounts for the
427 remaining observed longitudinal cell deformation, ultimately accounting for most of the
428 longitudinal cell deformation observed during osmotic expansion. The foil model illustrates this
429 crucial influence of cell geometry on longitudinal extensibility. Though foil cells were materially
430 isotropic and lacked directional reinforcements, they increased in length dramatically when
431 pressurized internally via a purely geometric bellows-like mechanism. This length increase
432 occurred without a corresponding increase in radius, qualitatively mimicking the deformations of
433 parenchyma cells subjected to increased turgor.

434 Foil models were capable of recapitulating anisotropic expansion; however, we observed
435 material failure in these physical models following repeated cycles of expansion and contraction.
436 Counterintuitively, inflated foil cells displayed kinking of their perimeters when pressurized
437 internally; a product of cell radii decreasing slightly and cell circumferences being drawn into
438 compression as a necessary consequence of elongation with constant surface area. Analogous
439 invaginations have been described previously in the walls of turgid plant cells and are
440 suggested to play a role in the generation of lobed cell morphologies by generating stress
441 hotspots (Bidhendi et al., 2019). In the foil models, circumferential kinks were often sites of
442 material failure and rupture, presumably resulting from repeated concentration of stress and
443 material fatigue. Extending this analogy to biological parenchyma cells, we suggest that in
444 addition to facilitating anisotropic stretching of cell walls in the longitudinal direction, the
445 flexibility of the cell wall imparted by unidirectional cellulose reinforcement is functionally

important as a means of mitigating stress concentrations that have the potential to damage constantly deforming parenchyma cells. Like those of growing plant cells, the cell walls of hydraulically deformable parenchyma must be stiff enough to withstand internal turgor pressure but not so stiff as to restrict turgor-driven deformation. Pulvinus parenchyma, however, faces the additional challenge that it must deform repeatedly over the lifetime of a plant without sustaining material damage significant enough to rupture cells. Accordingly, we suggest that both cell wall reinforcement and cell geometry are essential to the operation of *M. pudica* pulvini, as neither specialization in isolation could produce both the magnitude of cell deformation required for physiologically useful motion and the durability necessary for repetitive use.

Functional interdependence of cell anisotropy and epidermis reinforcement

Most plant stems and petioles are ensheathed in a skin of elongate epidermis cells oriented parallel to the growth axis of the organ (Kutschera, 2008). This parallel orientation of epidermal cells is a natural consequence of turgor-driven morphogenesis, in which elongated plant organs form developmentally through anisotropic expansion and elongation of the cells that compose them. Over most of their lengths, the petioles of *M. pudica* display a typical epidermis morphology of elongate cells oriented parallel to the organ long axis. In the immediate regions of pulvini, however, we observed epidermis cells oriented perpendicular to the growth axis. Cell orientation has been shown to have a direct effect on the material stiffness of plant epidermis, inducing anisotropic tensile properties and relatively lower tensile stiffness in the direction perpendicular to the orientation of epidermal cells (Bidhendi et al., 2020). Additionally, a perpendicular orientation of epidermis cells facilitates the formation of wrinkles transverse to the long axis of the pulvinus. Like wrinkles on the surfaces of mammalian finger and elbow joints, transverse wrinkles in the pulvinus epidermis provide extra surface area that can be

extended or contracted at low force (Song et al., 2014), ultimately allowing the epidermis to strain longitudinally at low force without sacrificing circumferential stiffness.

In the absence of an enveloping epidermis, we observed outward bowing of osmotically swollen parenchyma tissue away from the central axis of cylindrical pulvinus sections. This parenchymal bowing likely results from a difference in the longitudinal extensibility of parenchyma tissues and the vascular elements they surround. Isolated parenchyma tissues dissected away from the mechanical context of the pulvinus organ display a strong bias for purely longitudinal expansion; however, when coupled to a relatively stiff vasculature core in the context of an intact organ, pure longitudinal expansion along a straight line is resisted, and outward curvature of longitudinally expanding parenchyma tissue results. This phenomenon does not occur when the epidermis is present, indicating that the circumferential stiffness of the epidermis resists outward bowing of parenchyma tissues. While cell wall reinforcement and cell geometry ensure longitudinal expansion of individual parenchyma cells, the epidermis mitigates radial deformations that emerges at higher scales of tissue organization, ensuring that hydraulic expansion of parenchyma tissue *en masse* remains aligned along the long axis of the pulvinus.

Physical models provide insight into the effects of structural constraints on mechanical efficiency

The silicone physical models demonstrate the potential for circumferential reinforcements to influence the energetic cost of hydraulic bending. Bulk movement of fluid within pulvini is ultimately driven by osmotic and hydrostatic pressure gradients generated through active transport of ions and other osmolites against their concentration gradients (Scorza and Dornelas, 2011; Wang and Li, 2020). Forming and maintaining these gradients is an energy intensive process powered by hydrolyzation of ATP to ADP (Fromm and Eschrich, 1988a) and

494 incurs a physiologically relevant metabolic cost. *M. pudica* plants induced to fold at excessive
495 frequency display a decreased investment in reproductive growth, indicating a reallocation of
496 metabolic energy from reproduction to movement (Bao et al., 2018). Plants subjected to
497 constant mechanical stimuli selectively reduce their touch response in advance of the onset of
498 fatigue (Amador-Vargas et al., 2014; Abramson and Chicas-Mosier, 2016), indicating that
499 behavioral adaptations have evolved to limit excessive actuation. In our silicone models,
500 transverse sewing thread hoop reinforcements provide a mechanical means of reducing the
501 energetic cost of movement by decreasing the volume of fluid transfer required to effect
502 bending. Extending this analogy to biological pulvini, we suggest that anisotropic reinforcement
503 of the parenchyma cell wall, longitudinally flattened spheroidal cell geometries, and
504 perpendicular orientations of epidermal cells are all morphological specializations that function
505 in concert to reduce the energetic cost of hydraulic movement. By passively restricting
506 unproductive radial expansion, these structures reduce the volume of hydraulic fluid that must
507 be displaced via active formation of osmotic gradients, ultimately reducing the metabolic energy
508 that pulvinus-bearing plants must dedicate to motor functions.

509 Restrictions to unproductive radial expansion likely also influence the speed of pulvinus
510 bending. Thigmonastic leaf movement in the sensitive plant *Mimosa pudica* is among the fastest
511 movements displayed by plants, and one of the fastest purely hydraulic movements known in all
512 of biology (Skotheim and Mahadevan, 2005). The minimum duration of any hydraulic movement
513 will equal the maximum speed at which fluid transport can occur multiplied by the volume of fluid
514 that must be displaced to complete the movement. In plant tissues, the maximum rates of
515 hydraulic fluid movement are limited by the speeds at which osmotic gradients can be
516 generated biochemically (Morillon et al., 2001) and by physical limitations to the speeds at
517 which hydrostatic pressures can equilibrate via movement of fluid within a porous medium
518 (Skotheim and Mahadevan, 2005; Forterre, 2013). Reducing unproductive radial bulging

presents a structural means of reducing the amount of fluid that must be transferred to induce a given degree of hydraulic bending, thus decreasing the amount of time required to induce hydraulic actuation, and ultimately increasing the speed of bending. The impressive speeds of pulvinus driven movements in sensitive plants are known to depend on exceptionally rapid solute redistribution mechanisms (Morillon et al., 2001), and here we illustrate that the evolution of structural systems that guide hydraulic deformation may be an equally crucial, but largely overlooked, aspect of rapid plant motor mechanics.

Towards a generalized framework for characterizing biological motor organs

Biological motor organs accomplish two distinct functions: they convert stored potential energy into the kinetic energy of motion, and they guide the expression of that kinetic energy towards accomplishment of a physiologically relevant motor task. In the case of a pulvinus, conversion of energy occurs at the subcellular level where chemical potential energy is converted into movement of solutes and, subsequently, water by the action of ATP-hydrolyzing membrane pumps (Lyubimova et al., 1964; Scorza and Dornelas, 2011). As shown in the current study, conversion of the resulting isotropic cell deformation into anisotropic tissue and organ deformation is then a product of a reinforcing extracellular matrix of parenchymal and epidermal cell walls. This pattern of subcellular energy transformation and extracellular structural guidance is not unique to pulvini. In vertebrate skeletal muscle, conversion of chemical potential to kinetic energy is accomplished via ATP-powered interactions between actin and myosin motor proteins housed within contractile muscle fibers (Cain and Davies, 1962; Rall, 2014). Coordination of the action of hundreds or thousands of contracting muscle fibers towards purposeful deformation of the entire organ, however, is a product of the collagenous extracellular matrix that reinforces muscle. The collagenous extracellular matrix surrounds and connects muscle fibers, ultimately linking them to in-series tendons and providing

544 a pathway for both internal and external transmission of force (Purslow, 2020). Interactions
545 between the matrix and the contractile cells it surrounds influences the speed and force of
546 active contraction (Eng et al., 2018; Sleboda and Roberts, 2020), as well as the material
547 stiffness of muscle tissue (Gindre et al., 2013; Sleboda and Roberts, 2017).

548 A paradigm of cellular energy transformers embedded in a guiding fibrous matrix
549 provides a useful framework in which to analyze both biological motor organs and engineered
550 biologically inspired actuators. Researchers studying biological motor organs and engineers
551 designing bioinspired systems can consider not only the mechanisms of energy conversion
552 employed by individual actuating elements, but also the means by which an investing matrix or
553 harnessing system facilitates coordinated action and the emergence of novel behaviors at
554 higher levels of organization. McKibben artificial muscles, for example, are a class of
555 engineered actuator that contains a pneumatically expandable tube surrounded by a sleeve of
556 braided fibers. Depending on the orientation of sleeve fibers, McKibben actuators can be made
557 to either forcibly elongate or forcefully shorten when pressurized internally (Chou and
558 Hannaford, 1996). Precise engineering of sleeve architecture has increased the complexity of
559 motions performable by McKibben-like actuators (Singh and Krishnan, 2017), and incorporation
560 of multiple McKibben actuators into an array has yielded complex automatic gearing behavior
561 not displayed by individual actuators (Azizi and Roberts, 2013). These emergent behaviors
562 represent a form of structural intelligence encoded mechanically via the coupling of an
563 increasingly complex reinforcing matrix to a simple pneumatically inflated system. Such
564 strategies provide a means of reducing the need for complex control inputs to achieve complex
565 motion, and thus are conducive to the design of engineered actuators with limited top-down
566 control and to the emergence of biomechanical systems that can operate largely in the absence
567 of direct neural control. Here we provide a natural example of this strategy. Through interaction
568 of energy-transforming hydraulic cells and structural guidance encoded in the structure of cell

walls and epidermis, pulvinus-bearing plants transform simple expansion and contraction of hydraulic cells into rapid, repeatable, and directed movement of their parts.

Acknowledgements

We thank Youssef Chebli for help in microscope operation and helpful discussions about data collection, and David Liu and S. Kelly Sears at the Facility for Electron Microscopy Research of McGill University for help in microscope operation and data collection.

Funding

Funded by a Human Frontier Science Program long-term postdoctoral fellowship (LT - 000531/ 2020).

Competing Interests

We have no competing interests to declare.

Source Data Files

Figure 2- Source Data 1: Histogram data- Tabulated Cellulose Orientations

Figure 3- Source Data 1: Tabulated Dimensions of Pulvinus Tissue Sections in Graded Osmotic Baths

Figure 4- Source Data 1: Tabulated Dimensions of Individual Parenchyma Cells in Osmotically Neutral and Osmotically Hypotonic Baths

590 **Videos**

591 Figure 3- Video 1: 30-minute timelapse video illustrating osmotic expansion of a cylindrical
592 section of pulvinus. Organ section is shown in lateral view.

593 Figure 3-Video 2: 15-minute timelapse video illustrating osmotic expansion of a cylindrical
594 section of pulvinus skinned of its enveloping epidermis. Note bowing of dorsal and ventral
595 surfaces. Organ section is shown in lateral view.

596 Figure 3- Video 3: 20-minute timelapse video illustrating osmotic expansion of a rectangular
597 block of parenchyma tissue. Tissue is shown in dorsal view.

598 Figure 5- Video 1: Hydraulically pressurizing one side an unreinforced pulvinus physical model.

599 Video S5: Hydraulically pressurizing one side of a pulvinus physical model reinforced by sewing
600 thread hoops.

601 Video S6: Pneumatic expansion of a foil model of serially connected parenchyma cells.

602

603 **References Cited**

604 Abramson, C. I. and Chicas-Mosier, A. M. (2016). Learning in plants: lessons from *Mimosa*
605 *pudica*. *Front. Psychol., 7*, 417. 10.3389/fpsyg.2016.00417.

606 Adamski, M., Fontana, G., Gershlak, J. R., Gaudette, G. R., Le, H. D. and Murphy, W. L. (2018).
607 Two methods for decellularization of plant tissues for tissue engineering applications. *J.*
608 *Vis. Exp.*, 135, e57586. 10.3791/57586.

609 Amador-Vargas, S., Dominguez, M., León, G., Maldonado, B., Murillo, J. and Vides, G. L.
610 (2014). Leaf-folding response of a sensitive plant shows context-dependent behavioral
611 plasticity. *Plant Ecol., 215*(12), 1445-1454. 10.1007/s11258-014-0401-4.

612 Aylor, D. E., Parlange, J. Y. and Krikorian, A. D. (1973). Stomatal mechanics. *Am. J. Bot., 60*(2),
613 163-171. 10.1002/j.1537-2197.1973.tb10213.x.
614 Azizi, E. and Roberts, T. J. (2013). Variable gearing in a biologically inspired pneumatic actuator
615 array. *Bioinspir. Biomim., 8*(2), 026002. 10.1088/1748-3182/8/2/026002.
616 Bao, T., Roy, G. and Cahill Jr, J. F. (2018). Photosynthetic opportunity cost and energetic cost
617 of a rapid leaf closure behavior in *Mimosa pudica*. *Am. J. Bot., 105*(9), 1491-1498.
618 10.1002/ajb2.1154.
619 Baskin, T. I. (2005). Anisotropic expansion of the plant cell wall. *Annu. Rev. Cell Dev. Biol., 21*,
620 203-222. 10.1146/annurev.cellbio.20.082503.103053.
621 Bidhendi, A. J., Altartouri, B., Gosselin, F. and Geitmann, A. (2019). Mechanical stress initiates
622 and sustains the morphogenesis of wavy leaf epidermal cells. *Cell Rep., 28*(5), 1237-
623 1250. 10.1016/j.celrep.2019.07.006.
624 Bidhendi, A. J., Chebli, Y. and Geitmann, A. (2020). Fluorescence visualization of cellulose and
625 pectin in the primary plant cell wall. *J. Microsc., 278*(3), 164-181. 10.1111/jmi.12895.
626 Bidhendi, A. J. and Geitmann, A. (2016). Relating the mechanics of the primary plant cell wall to
627 morphogenesis. *J. Exp. Bot., 67*(2), 449-461. 10.1093/jxb/erv535.
628 Bidhendi, A. J., Li, H. and Geitmann, A. (2020). Modeling the nonlinear elastic behavior of plant
629 epidermis. *Botany, 98*(1), 49-64. 10.1139/cjb-2019-0058.
630 Brett, C. T. (2000). Cellulose microfibrils in plants: biosynthesis, deposition, and integration into
631 the cell wall. *Int. Rev. Cytol.,* 199, 161-199. 10.1016/S0074-7696(00)99004-1.
632 Cain, D. and Davies, R. (1962). Breakdown of adenosine triphosphate during a single
633 contraction of working muscle. *Biochem. Biophys. Res. Commun., 8*(5), 361-366.
634 10.1016/0006-291X(62)90008-6.
635 Chou, C.-P. and Hannaford, B. (1996). Measurement and modeling of McKibben pneumatic
636 artificial muscles. *IEEE Trans. Robot., 12*(1), 90-102. 10.1109/70.481753.
637 Darwin, C. and Darwin, F. (1880). *The power of movement in plants*. Appleton, New York, NY.

Eng, C. M., Azizi, E. and Roberts, T. J. (2018). Structural Determinants of Muscle Gearing During Dynamic Contractions. *Integr. Comp. Biol., 58*(2), 207-218. 10.1093/icb/icy054.

Forterre, Y. (2013). Slow, fast and furious: understanding the physics of plant movements. *J. Exp. Bot., 64*(15), 4745-4760. 10.1093/jxb/ert230.

Forterre, Y., Skotheim, J. M., Dumais, J. and Mahadevan, L. (2005). How the Venus flytrap snaps. *Nature, 433*(7024), 421-425. 10.1038/nature03185.

Franks, P. J. (2003). Use of the pressure probe in studies of stomatal function. *J. Exp. Bot., 54*(387), 1495-1504. 10.1093/jxb/erg162.

Fromm, J. and Eschrich, W. (1988a). Transport processes in stimulated and non-stimulated leaves of *Mimosa pudica*. *Trees, 2*(1), 7-17. 10.1007/BF00196974.

Fromm, J. and Eschrich, W. (1988b). Transport processes in stimulated and non-stimulated leaves of *Mimosa pudica*. *Trees, 2*(1), 18-24. 10.1007/BF00196975.

Galatis, B. and Apostolakos, P. (2004). The role of the cytoskeleton in the morphogenesis and function of stomatal complexes. *New Phytol., 161*(3), 613-639. 10.1046/j.1469-8137.2003.00986.x.

Gibson, L. J. (2012). The hierarchical structure and mechanics of plant materials. *J. R. Soc. Interface, 9*(76), 2749-2766. 10.1098/rsif.2012.0341.

Gindre, J., Takaza, M., Moerman, K. M. and Simms, C. K. (2013). A structural model of passive skeletal muscle shows two reinforcement processes in resisting deformation. *J. Mech. Behav. Biomed. Mater., 22*, 84-94. 10.1016/j.jmbbm.2013.02.007.

Kagawa, H. and Saito, E. (2000). A model on the main pulvinus movement of *Mimosa pudica*. *JSME Int. J. C-Mech Sy., 43*(4), 923-928. 10.1299/jsmec.43.923.

Koller, D. and Zamski, E. (2002). The phototropic pulvinus of bean *Phaseolus vulgaris L.*-Functional features. *Plant Biol., 4*(5), 584-594. 10.1055/s-2002-35442.

662 Kumon, K. and Suda, S. (1984). Ionic Fluxes from Pulvinar Cells during the Rapid Movement of
663 *Mimosa pudica L. Plant. Cell. Physiol., 25*(6), 975-979.
664 10.1093/oxfordjournals.pcp.a076813.
665 Kutschera, U. (2008). The growing outer epidermal wall: design and physiological role of a
666 composite structure. *Ann. Bot., 101*(5), 615-621. 10.1093/aob/mcn015.
667 Kwan, K., Ye, Z., Chye, M. and Ngan, A. (2013). A mathematical model on water redistribution
668 mechanism of the seismonastic movement of *Mimosa pudica*. *Biophys. J., 105*(1), 266-
669 275. 10.1016/j.bpj.2013.06.001.
670 Liu, Z. Q. (1991). Scale space approach to directional analysis of images. *Appl. Opt., 30*(11),
671 1369-1373. 10.1364/AO.30.001369.
672 Lyubimova, M.N., Demianovskaya, N.C., Fedorovich, I.B., and Itomlenskyte, I.V. (1964). The
673 part played by ATP in the motor function of the *Mimosa pudica* leaf (in Russian).
674 *Biokhymya, 29*(4), 774-779.
675 Mano, H. and Hasebe, M. (2021). Rapid movements in plants. *J. Plant. Res., 134*(1), 3-17.
676 10.1007/s10265-020-01243-7.
677 Mayer, W.-E., Flach, D., Raju, M., Starrach, N. and Wiech, E. (1985). Mechanics of circadian
678 pulvini movements in *Phaseolus coccineus L*. *Planta, 163*(3), 381-390.
679 10.1007/BF00395147.
680 Minorsky, P. V. (2019). The functions of foliar nyctinasty: a review and hypothesis. *Biol. Rev.,*
681 *94*(1), 216-229. 10.1111/brv.12444.
682 Morillon, R., Liénard, D., Chrispeels, M. J. and Lassalles, J.-P. (2001). Rapid movements of
683 plants organs require solute-water cotransporters or contractile proteins. *Plant Physiol.,*
684 *127*(3), 720-723. 10.1104/pp.010732.
685 Purslow, P. P. (2020). The structure and role of intramuscular connective tissue in muscle
686 function. *Front. Physiol., 11*, 495. 10.3389/fphys.2020.00495.

Rall, J. A. (2014). *Mechanism of muscular contraction*: Springer, New York, NY. 10.1007/978-1-4939-2007-5.

Satter, R. L., Sabnis, D. D. and Galston, A. W. (1970). Phytochrome controlled nyctinasty in *Albizzia julibrissin*. I. Anatomy and fine structure of the pulvinule. *Am. J. Bot., 57*(4), 374-381. 10.1002/j.1537-2197.1970.tb09826.x.

Schindelin, J., Arganda-Carreras, I., Frise, E., Kaynig, V., Longair, M., Pietzsch, T., Preibisch, S., Rueden, C., Saalfeld, S., Schmid, B., Tinevez, J. Y., White, D. J., Hartenstein, V., Eliceiri, K., Tomancak, P. and Cardona, A. (2012). Fiji: an open-source platform for biological-image analysis. *Nat. Methods, 9*(7), 676-682. 10.1038/nmeth.2019.

Scorza, L. C. T. and Dornelas, M. C. (2011). Plants on the move: towards common mechanisms governing mechanically-induced plant movements. *Plant Signal. Behav., 6*(12), 1979-1986. 10.4161/psb.6.12.18192.

Singh, G. and Krishnan, G. (2017). A constrained maximization formulation to analyze deformation of fiber reinforced elastomeric actuators. *Smart Mater. Struct., 26*(6), 065024. 10.1088/1361-665X/aa6dc6.

Skotheim, J. M. and Mahadevan, L. (2005). Physical limits and design principles for plant and fungal movements. *Science, 308*(5726), 1308-1310. 10.1126/science.1107976.

Sleboda, D. A. and Roberts, T. J. (2017). Incompressible fluid plays a mechanical role in the development of passive muscle tension. *Biol. Lett., 13*(1), 20160630. 10.1098/rsbl.2016.0630.

Sleboda, D. A. and Roberts, T. J. (2020). Internal fluid pressure influences muscle contractile force. *Proc. Natl. Acad. Sci. USA, 117*(3), 1772-1778. 10.1073/pnas.1914433117.

Song, K., Yeom, E. and Lee, S. J. (2014). Real-time imaging of pulvinus bending *in Mimosa pudica*. *Sci. Rep., 4*, 6466. 10.1038/srep06466.

Taiz, L., Zeiger, E., Møller, I. M. and Murphy, A. (2015). *Plant physiology and development*: Sinauer Associates, Sunderland, CT.

Tamiya, T., Miyazaki, T., Ishikawa, H., Iriguchi, N., Maki, T., Matsumoto, J. J. and Tsuchiya, T. (1988). Movement of water in conjunction with plant movement visualized by NMR imaging. *J. Biochem., 104*(1), 5-8. 10.1093/oxfordjournals.jbchem.a122421.

Wang, Y. and Li, H. (2020). Bio-chemo-electro-mechanical modelling of the rapid movement of Mimosa pudica. *Bioelectrochemistry, 134*, 107533. 10.1016/j.bioelechem.2020.107533.

719 **Figure Legends (duplicated from above)**

720 Figure 1: Epidermal cells are oriented perpendicular to the pulvinus long axis and associated
721 with transverse surface wrinkles. [A] Line drawing depicting the locations of primary (B),
722 secondary (C), and tertiary (D) pulvini of *Mimosa pudica*. [B,C,D] Scanning electron
723 micrographs of pulvinus surfaces identified in [A]. Inset micrographs show epidermis
724 architecture at higher magnifications. Epidermis cells bounding pulvini are roughly cylindrical in
725 shape and oriented perpendicular to the long axes of organs. Wrinkles in the epidermis form
726 preferentially parallel to the long axes of epidermis cells. [E] Epidermis cell orientation
727 transitions from perpendicular in the region of the pulvinus to parallel in the region of the petiole
728 (note that the organ long axis is oriented vertically in panel E).

729

730 Figure 2: Cellulose microfibrils reinforcing parenchymal cell walls are oriented perpendicular to
731 the pulvinus long axis. [A] Scanning electron micrograph showing a lateral view of a
732 longitudinally bisected primary pulvinus. Protoplasts have been removed chemically to reveal
733 cell wall architecture. Labels indicate dorsal (adaxial) epidermis (d.e.), dorsal parenchyma (d.p.),
734 vasculature (vasc.), ventral (abaxial) parenchyma (v.p.), and ventral epidermis (v.e.). Organ is
735 oriented with petiole (pet.; not visible) left of the frame. [B] Magnified view of the highlighted
736 region in A showing ventral parenchyma bounded by vasculature and ventral epidermis. [C]
737 Magnified view of the highlighted region in B showing the inner face of one parenchymal cell
738 wall. [D] High magnification view of the highlighted region in C showing cellulose microfibrils
739 running primarily dorso-ventrally in the plane of the cell wall. Fiber angles are described relative
740 to the long axis of nearby vasculature (defined as 0°) with 90° indicating a perpendicular
741 orientation. [E] Histograms showing distributions of fiber orientations in 9 cells from 4 pulvini.
742 Each gray trace shows the distribution of fiber angles in a high magnification scanning electron
743 micrograph similar to D. A gaussian curve (solid red trace) fit to all histograms indicates a

744 predominant fiber orientation of 82.5 degrees (solid vertical line) with a standard deviation of ±
745 29.1 degrees (dotted vertical lines). Source data file provides tabulated histogram values.

746

747 Figure 3: Nonuniform osmotic swelling of pulvini reveals multiscale control of hydraulic
748 deformation. [A] Lateral view of an intact *Mimosa pudica* primary pulvinus with flanking leaves
749 removed. Dashed white lines illustrate cross-sectional cuts used to isolate a cylindrical section
750 of pulvinus. Orange arrowheads in A and C indicate proximal, ventral corner of section. [B]
751 Isolated cylindrical section of pulvinus with epidermis partially removed to illustrate skinning
752 technique. [C, D, E] Effect of graded osmotic bathing solutions on the length (L, black circles),
753 cross-sectional width (w, blue squares), and height (h, red diamonds) of excised pulvinus
754 sections. Inset line drawings depict dimensions and typical morphologies in lateral and cross-
755 sectional views. Graph markers are means ± SD normalized to tissue dimensions in the most
756 hypertonic bathing solution (878 mOsm). Asterisks denote values significantly different from 1.0
757 in the most hypotonic bathing solution (0 mOsm). [C] Isolated pulvinus sections expand
758 longitudinally in increasingly hypotonic bathing solutions with negligible change in width or
759 height. [D] Sections manually skinned of their epidermis expand primarily in length but display a
760 small increase in width and increased variability in height. [E] Isolated blocks of parenchyma
761 tissue expand longitudinally with negligible change in width or height. Sample sizes (n) for each
762 condition are noted beside inset illustrations. [F] Representative images illustrating shape
763 changes of pulvinus sections in each state of dissection. Upper and lower images of each pair
764 display sample shape in hypertonic and hypotonic baths, respectively. Scale bars 500 μm.
765 Associated videos show timelapses of osmotic deformations. Source data file provides
766 tabulated dimensions in each osmotic condition.

767

768 Figure 4: Nonuniform osmotic swelling of pulvinus parenchyma cells reveals mechanical
769 anisotropy in the cell wall. [A] Confocal micrographs of parenchyma tissue imaged in osmotically
770 isotonic (384 mOsm) and hypotonic (distilled H_2O) bathing solutions. Representative
771 micrographs show cell morphology as seen in frontal and lateral views. All scale bars 20 μm.
772 Inset line drawings illustrate changes in cell shape between osmotic solutions. [B] Effect of
773 osmotic swelling on frontal and lateral dimensions of 53 cells measured over 8 experimental
774 trials. Gray dots represent percent changes in cell dimensions following transfer from neutral to
775 hypotonic bath. Black markers represent means ± standard errors. Asterisks denote percent
776 changes significantly different from zero ($p<0.05$). Source data file provides tabulated
777 dimensions in each osmotic condition.

778

779 Figure 5: Physical models of gross pulvinus structure illustrate the influence of shape
780 constraints on hydraulic and energetic bending efficiencies. [A] An abstracted physical model of
781 a pulvinus made of flexible silicone rubber. Transfer of water from one half of the model to the
782 other causes long-axis bending. [B] Sewing thread hoop reinforcements prevent radial
783 expansion of pressurized model chambers. [C] Lateral view of a longitudinally bisected primary
784 pulvinus organ. Opposing silicone chambers of each model represent dorsal (dp) and ventral
785 (vp) parenchyma cell groups, respectively. Pulvinus vasculature (v) and petiole (p) indicated for
786 clarity. [D, E, F] Comparison of fluid volume, pressure, and work required to effect a change in
787 bending angle in an unreinforced (open circles) and a hoop-reinforced (filled circles) physical
788 model. Graphs in left-hand column describe bending phase of motion for each model, while
789 graphs in shaded right-hand column describe return phase of motion. Asterisks in inset line
790 drawings indicate expanding halves of models in each movement phase. [D] The volume of fluid
791 required to effect angle change is reduced in the reinforced model relative to the unreinforced
792 model during both bend and return motions. [E] Fluid pressures measured from expanding

model compartments are elevated in the reinforced model. [F] Mechanical work (the integral of pressure and volume changes) expended transferring water across model compartments is ultimately lower for the reinforced model during both bending and returning phases of motion. Associated videos show models bending hydraulically.

Figure 6: A mylar foil model of parenchyma cells demonstrates the influence of cell geometry on mechanical anisotropy. [A] The model is composed of eight flattened, hexagonal cells connected serially. Foil cell walls lack directional reinforcements and are inextensible and materially isotropic. [B] When pressurized internally, cells extend longitudinally with negligible change in radius. [C] Kinks formed in inextensible cell walls result in material failure and loss of pressurization following repeated cycles of expansion and contraction. Associated video shows pneumatic expansion of the model.